International Forum on Aeroelasticity and Structural Dynamics
IFASD 2019
9-13 June 2019, Savannah, Georgia, USA

ANALYSIS OF A SLOSHING BEAM EXPERIMENT

Branislav Titurus[1], Jonathan E. Cooper[1], Francesco Saltari[2], Franco Mastroddi[2], Francesco Gambioli[3]

[1] University of Bristol
University Walk, Bristol, BS8 1TR, England, U.K.
brano.titurus@bristol.ac.uk
j.e.cooper@bristol.ac.uk

[2] Sapienza University of Rome
Via Eudossiana 18, 00184 Rome, Italy
francesco.saltari@uniroma1.it
franco.mastroddi@uniroma1.it

[3] Airbus Operations Ltd
Pegasus House, Aerospace Avenue, Filton, Bristol, BS43 7PA, England, U.K.
francesco.gambioli@airbus.com

Keywords: damping, identification, fluid-structure interaction, sloshing, experiment.

Abstract: Fuel sloshing is seen as a potential mechanism to reduce the loads in aircraft due to atmospheric turbulence and gusts via an increase in the effective damping. A series of step-release experiments have been performed on a cantilever beam structure with a tank at its end filled with different levels of liquid in order to provide experimental data to characterise the amount of damping caused by the sloshing motion and to validate future numerical models. This paper presents an analysis of some of the acceleration data sets acquired during the experiments and shows how the frequency and damping behaviour varies during the time decay resulting from the step-release. Correlation is made between the amount of effective damping and the different fluid motions in the tank. The analysis is repeated for the dry beam configurations as well as different test conditions including tank level filling and number of compartments in the tank.

1 INTRODUCTION

There is a continuing drive to improve the performance of civil jet airliners and contribute towards establishing more eco-friendly air transport. One approach to achieve this goal is to use some form of loads alleviation in order to reduce the effect of turbulence, gusts and manoeuvres which leads to a subsequent reduction in structural weight. Many different types of approaches have been used to achieve this goal, including aerodynamic approaches using control surfaces or spoilers, or structural methods such as aeroelastic tailoring.

In Civil Engineering there have been many cases of using some form of fluid in a tank as a tuned mass damper to reduce the response of tall buildings to the wind or earthquakes [1], [2]. Little work has been done in using such an approach for civil aircraft with preliminary studies only considering the motions of a tank on seismic shaking table with little consequent vertical motion as would be expected from a wing undergoing complex responses due to gust excitation [3], [4]. Further, it was shown experimentally that large amplitude response of the full-scale empty wing already features significant nonlinear damping effects [5].

As part of a wider project, a number of experiments have recently been performed at the *Airbus Protospace Lab* in Filton (Bristol, UK) to explore the effects of a tip tank containing a fluid on the motion of a beam subjected to moderate initial deflections and the subsequent release [6]. The objective of this preliminary campaign was to show that liquid sloshing affects significantly the damping characteristics of a free-vibrating wing-like structure, and therefore has the potential of alleviating dynamics loads if taken into account in the modelling.

This paper is organized as follows: after initial motivation, chapter 2 provides an overview of the experimental configuration and a suite of methods applied for dynamics identification. Then, chapter 3 presents initial analysis of the typical measured responses combined with the identification and model-based analysis of the underlying modal behaviour during small vibrations. Finally, motivated by the preliminary analysis, chapter 4 provides a more focused time-frequency analysis of the key identified dynamic propertied across a range of the test conditions. Conclusions summarize the key findings, insights and outlook for further research.

2 METHODS

2.1 Experimental set-up

The structural set-up is shown in Figure 1. The main structural member is a cantilevered steel beam of 2.35 m span made from standard universal H-section steel joist 127×76×13. A modular liquid tank spanning the last 0.7 m is mounted in four discrete locations onto the beam at the free end. Based on the selected scaling strategy, the water-cantilever mass ratio is ~7 %, which is representative of a civil aircraft with reserve fuel [6]. The cantilever is equipped with various motion, deformation and load sensors, including piezoelectric accelerometers at the free-end and a strain gauge close to the root which is attached to the rigid frame. A remotely controlled quick release mechanism was employed to pull the free-end down to a maximum deflection of approximately 4 % of the span, a condition close to maximum elastic stress in the beam, and suddenly release the beam.

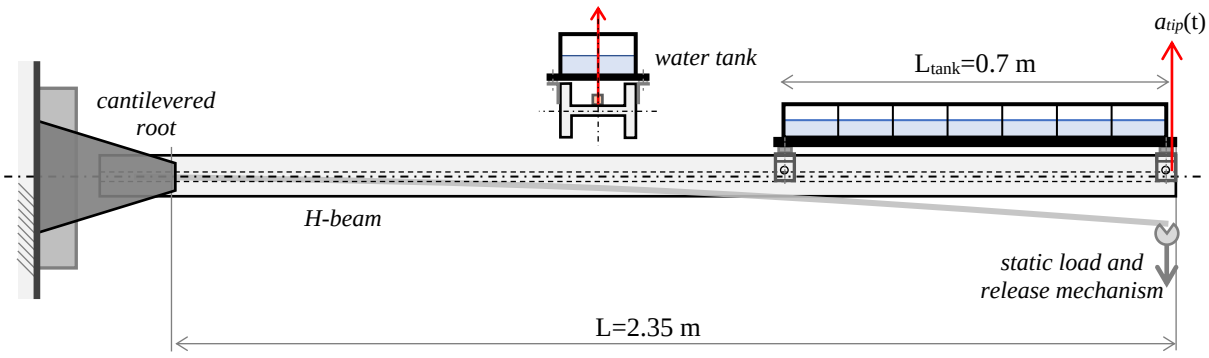

Figure 1: Experimental set-up.

The free oscillations of the system were then monitored and recorded. This work mostly focuses on the analysis of a single output channel which represents the transversal accelerations at the free end of the cantilever. However, several other acceleration and strain measurements were recorded during the test campaign. The signals were recorded with a sampling frequency of 1 kHz with a duration of 5 or 25 seconds. Additionally, high-speed videos, recorded at 3000 fps, of the liquid free-surface response within the tank were recorded to provide visual indication of the fluid-structure interaction conditions.

The experimental conditions studied in the research involved the following test variations:

- Impact-based free vibrations (tap) tests for nominal dry structure characterization,
- Initial deflection-release free vibrations for dry and wet fluid-structure analysis,
- Systematic tests with baffles (walls) and filling ratios: 20, 30, 40, 50, 60, 70, 80 %,
- Alternative test conditions (e.g. removed separating walls in the container).

Individual test configurations were typically tested three times. An extra effort was made to use different solid tuning masses to establish an identical fundamental frequency for all test cases with varying liquid content and the addition of extra test features (*e.g.* internal wall removal).

2.2 Research methodology

Initial deformation and subsequent release of the tested structure produced highly transient non-stationary free vibrations. The focus of this research is on the frequency content and amplitude of the decay trends in the measured data, and their changes with time. This investigation consists of preliminary and detailed analysis stages. Time and frequency domain tools are considered in both stages. Results of the preliminary stage inform selection of the tools for the detailed investigation. Owing to the specific nature of the excitation, and ignoring potential nonlinear effects due to moderate deflections, friction and other sources, it is anticipated that the initial conditions will introduce dynamic response characterized by the dominant participation of the fundamental bending mode of vibration. In this work, this vibration component is denoted **F1** while the next observed mode is denoted **F2**.

The *preliminary analysis* of the measured data involves inspection and mapping the complete raw time series as well as application of Fourier Transform techniques to facilitate frequency and time-frequency analyses. Standard tools such as a Fast Fourier Transform and Short-Time Fourier Transform (STFT) are used as implemented in Matlab [7].

To support the *detailed analysis* stage, three distinct techniques are applied to understand the time-evolving fluid-structure dynamics and the underlaying structural vibration properties. Initially, the Eigensystem Realisation Algorithm is used to characterize the dry structure under impact-induced small vibration conditions. Then, a Nonlinear Least Square fitting technique is used to study the time-varying properties of the fundamental vibration component **F1**. Finally, Wavelet Transform analysis is employed to study more closely the higher vibration component **F2** and its interaction with the fundamental component **F1**.

2.3 Identification methods

Eigensystem Realisation Algorithm (ERA) [8] is a classical time-domain Experimental Modal Analysis identification technique which can be used to estimate the natural frequencies, damping ratios, mode shapes and modal participation factors from uniformly sampled responses that are assumed to be the summation of decaying exponentially damped sinusoids. These signals can be generated from:

1. the response to an impulsive or step-release excitation, as used in this work,
2. the Impulse Response Function generated from the inverse Fourier Transform of the Frequency Response Function (FRF),
3. data manipulation of the response to an unknown random input, *e.g.* generating autocorrelations from the random input [9].

The decay responses are assumed to contain linear and time-invariant modal properties, although it can be possible to treat time varying systems by considering sections of the data separately.

Starting with the well-known discrete State Space equations using the usual notation

$$x_{j+1} = Ax_j + Bu_j \qquad and \qquad y_j = Cx_j + Du_j \tag{1}$$

where x_j, u_j and y_j are the system states, inputs and outputs respectively and *A*, *B*, *C* and *D* are the state, input, output and feedthrough matrices. The eigenvalues of the state matrix can be used to find the system frequencies and damping ratios.

For a Dirac impulse as the input, it can be shown that the so-called Markov equations result in the form

$$y_{j+1} = C\,A^j B \tag{2}$$

where *B* and *C* are vectors for the single input single output case. Defining the Hankel matrices such that

$$H_0 = \begin{bmatrix} y_1 & y_2 & y_3 & \cdots & y_\gamma \\ y_2 & y_3 & y_4 & \cdots & y_{\gamma+1} \\ y_3 & y_4 & y_5 & \cdots & y_{\gamma+2} \\ \vdots & \vdots & \vdots & \ddots & \vdots \\ y_\alpha & y_{\alpha+1} & y_{\alpha+1} & \cdots & y_{\alpha+\gamma+1} \end{bmatrix}, \quad H_1 = \begin{bmatrix} y_2 & y_3 & y_4 & \cdots & y_{\gamma+1} \\ y_3 & y_4 & y_5 & \cdots & y_{\gamma+2} \\ y_4 & y_5 & y_6 & \cdots & y_{\gamma+3} \\ \vdots & \vdots & \vdots & \ddots & \vdots \\ y_{\alpha+1} & y_{\alpha+2} & y_{\alpha+3} & \cdots & y_{\alpha+\gamma+2} \end{bmatrix} \tag{3}$$

and performing the Singular Value Decomposition (SVD) of the H_0 matrix as

$$H_0 = P\,S\,Q^T \tag{4}$$

then system realization theory [8] shows that the system matrix can be found, via use of the Markov equations (2), as

$$A = S^{-0.5} P^T H_1 Q\, S^{-0.5}\,. \tag{5}$$

This result is a so-called minimum realization estimate as the number of modes estimated by the solution depends upon the number of terms that are truncated from the matrix of singular values *S*; theoretically, the number of non-zero singular values are taken but these are not straightforward to determine on real experimental datasets and so a number of different truncation orders are considered.

Finally, the eigenvalues of system matrix *A*, λ, are related to the system frequencies and damping ratios by the expression

$$\lambda = \exp(\Delta t[\zeta\omega \pm j\omega\sqrt{1-\zeta^2}])\,. \tag{6}$$

It is also possible to deduce solutions for the *B* and *C* matrices but these will not be used in this work.

Nonlinear Least Squares (NLS) fitting technique is developed and used here to study the fundamental vibration component associated with the mode **F1** and its changes in time. Considering a typical full recorded time series of N_S samples, a sliding window consisting of N_W samples is used to form a time-localized data subset. An exponentially decaying single frequency function

$$s(t) = Ae^{-\delta t}\cos(2\pi f t + \varphi) \tag{7}$$

is parameterized such that the time-localized amplitude A, amplitude decay δ, frequency f and phase φ can be identified using the nonlinear least square fitting for each selected subset.

Given a suitable set of the initial parameter estimates and the sliding window specification, this procedure identifies an underlaying vibration component placed in the proximity of these initial estimates whilst filtering out the oscillatory effects attributed to the higher order system dynamics. Subsequent use of these optimized parameters in the following NLS iterations facilitates tracking of the changes in the identified parameters defined by equation (7).

A sampled acceleration signal $a(t_j)$ is divided into overlapping intervals $[t_i, t_i + \alpha(2\pi/\tilde{\omega}_{F1})]$ where t_i is the interval's starting time, $\tilde{\omega}_{F1}$ represents the initial value of the fundamental frequency **F1** and, typically, $\alpha \geq 1$. The following optimization problem is solved for time t_i

$$\min_{\mathbf{p}(t_i)} \sum_{(k)} \left(s(t_k - t_i; \mathbf{p}) - a(t_k) \right)^2, \quad t_k \in [t_i, t_i + \alpha(2\pi/\tilde{\omega}_{F1})] \tag{8}$$

to find $\tilde{\mathbf{p}}(t_i) = [A(t_i), \delta(t_i), f(t_i), \varphi(t_i)]$. The changes in $A(t_i)$ can be used to evaluate the vibration decay effects while $f(t_i)$ provides further insights into variations in **F1**.

The non-oscillatory part of equation (7) represents a line with the constant rate of decay δ when shown in a logarithmic scale, *i.e.* $\log Ae^{-\delta t} = \log A - \delta \cdot t$. This insight is the basis of the well-known Logarithmic Decrement approach used for damping identification [11]. The damping ratio can be obtained as $\zeta = \delta/(4\pi^2 f^2 - \delta^2)^{1/2}$. In combination with identified $f(t_i)$, either parameter $\delta(t_i)$ directly or $A(t_i)$ indirectly can be used to determine $\zeta(t_i)$. To enhance the robustness of this approach, linear interpolation applied to the values $\log A(t_i)$ on the chosen time intervals is used here to evaluate the measured damping trends.

Wavelet Transform (WT) technique [10] is a well-established technique used for detailed time-frequency analysis of non-stationary signals. If the STFT is performed by using a Fourier transform applied to a moving fixed-width window, WT is obtained by projecting signals onto a family of wavelets defined by dilating and moving a chosen mother wavelet by means of the so-called scale parameter *a* and a shift parameter τ:

$$CWT(a, \tau) = \int_{-\infty}^{\infty} \psi_{a,\tau}^{*}(t)\, x(t)\, dt \tag{9}$$

where

$$\psi_{a,\tau}(t) = \frac{1}{\sqrt{a}}\, \psi\left(\frac{t-\tau}{a}\right). \tag{10}$$

The direct link between the scale parameter *a* and frequency localization [10] enables a re-parametrization of the temporal scales into the frequencies to get an immediate reference to the dynamics of the considered unsteady process. In fact, WT uses larger wavelets in time to capture the low frequency behaviour and shorter wavelets to capture the high frequency content as well. Figure 2 shows how the time-frequency resolution of WT is not constant over its time-frequency domain. This is not the case of STFT. The low frequency content is featured by a better frequency resolution as well as a worse time-localization with respect to the high frequency content that, in turn, is featured by a low frequency resolution and a good time localization.

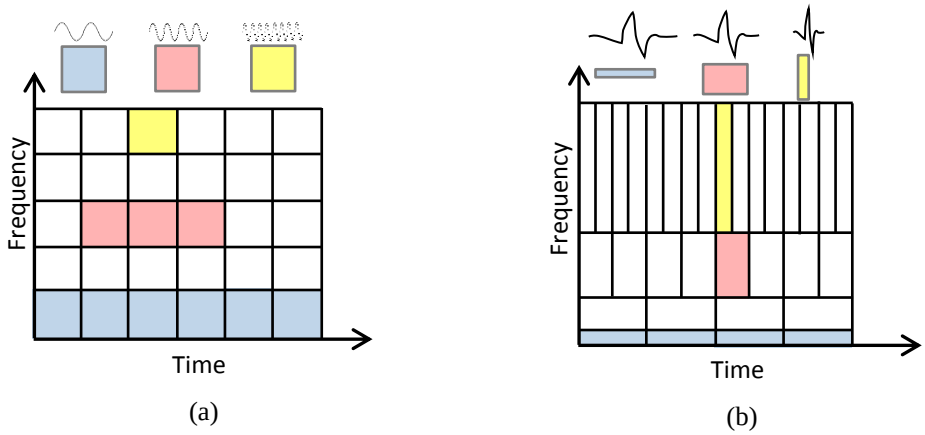

Figure 2: Time-Frequency representation of (a) STFT, (b) WT.

In this work, WT is used to show the unsteady nonlinear effects of a tank structure due to sloshing dynamics of internal fluid. More specifically, the modulation of the second mode amplitude and frequency are studied in detail. Such a modulation is featured at the frequency of **F1**, that is, the response of the first vibration bending mode. Within this framework, WT provides a complementary view to that of the STFT since it enables to detect the fast variations of frequency and response amplitude of **F2** rather than their trend.

WT transform provides a 2-D spectrum. Thus, an interpolation of WT spectrum based on a combination of 1-D frequency dependent Gaussian functions is performed for an arbitrary time instant in order to track the modal structural response parameters. Indeed, for each time shift value τ_k, the least square minimization problem is performed

$$\min_{A_n(\tau_k),\sigma_n(\tau_k),\nu_n(\tau_k)} \sum_{j=1}^{N_f} \left(\sum_{n=1}^{2} \frac{A_n(\tau_k)}{\sqrt{2\pi}\,\sigma_n(\tau_k)} e^{-\frac{1}{2}\left(\frac{f-\nu_n(\tau_k)}{\sigma_n(\tau_k)}\right)^2} - CWT(f,\tau_k) \right)^2 \tag{11}$$

where A_n is the area under the Gaussian function (*i.e.* a quantification of the instantaneous power of the *n*-th mode of response), σ_n is the flare of the Gaussian (though this information is highly influenced by the non-constant frequency resolution of WT), whereas ν_n is the instantaneous identified frequency.

3 PRELIMINARY ANALYSIS

3.1 Experimental results preview

This section looks at a single test set of data to illustrate some of the response characteristics and to motivate further analysis. Figure 3 shows the typical measured transversal tip acceleration responses following the step release for the *dry* (empty fuel containers) and *wet* (40% water-fill) test configurations. Both configurations are dynamically matched by using suitable solid masses in the dry test case.

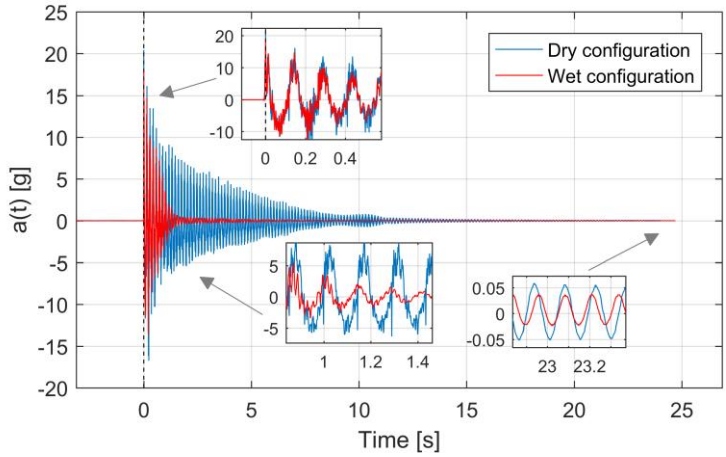

Figure 3: Dynamically matched time series for the dry and wet sloshing beam configurations.

The wet configuration features significantly faster free vibration decay compared to the dry case. Closer inspection of both time series indicates dominant participation of the fundamental bending modes **F1** with minor and fast decaying contributions from the higher bending modes. This wet configuration features at least two distinct vibration decay regions as well as an occurrence of a time shift between the two presented signals.

More detailed analysis is presented in Figure 4 based upon the STFT, as implemented in Matlab in function *spectrogram* [7]. These spectrograms use 512 sample windows with 500 sample overlap and the final spectra use zero-padding to the overall 2048 spectral lines.

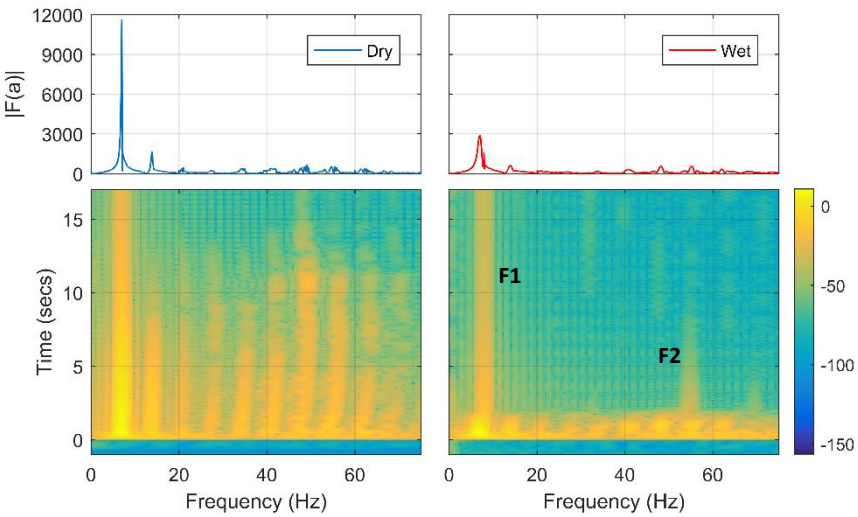

Figure 4: Frequency domain analysis of the selected dry and wet responses.

The top subplots of Figure 4 shows the half-spectra represented by the Fourier transform magnitude |F(a)| of the dry and wet configurations' full acceleration signals. Two closely spaced "twinned" peaks below 10 Hz suggest non-stationary nature of **F1** mode, while the repeated higher harmonic peaks can be attributed to the non-linearity in the dry structure. The bottom subplots of Figure 4 show these time-localized phenomena more clearly. The "peak-twinning" is linked to variation in **F1** as the acceleration amplitude reduces. This is particularly noticeable in the wet system during the initial strong liquid-structure interactions. The repeated higher harmonic patterns clearly present in the dry system are effectively damped in the wet system, revealing thus the underlying structural **F2** mode. The strongly non-stationary character of the wet configuration motivates further detailed time-localised signal analysis which commences with Experimental Modal Analysis identification of the reference dry configuration.

3.2 Reference modal analysis

Initial tap-tests were performed on the beam without fluid but with an added container and the tuning masses. The objective of these tests was to determine the repeatability of the results using tap-tests with a particular interest in the underlying damping inherent in the structure. The accelerations from the selected accelerometers along the beam were considered and the test was repeated 3 times. The original data that was sampled at 1 kHz was decimated by a factor of two, and then a low pass filter of 70 Hz was applied. Figure 5 shows selected parts of typical time histories and corresponding power spectra from the full time series for two accelerometers from one of the tap tests.

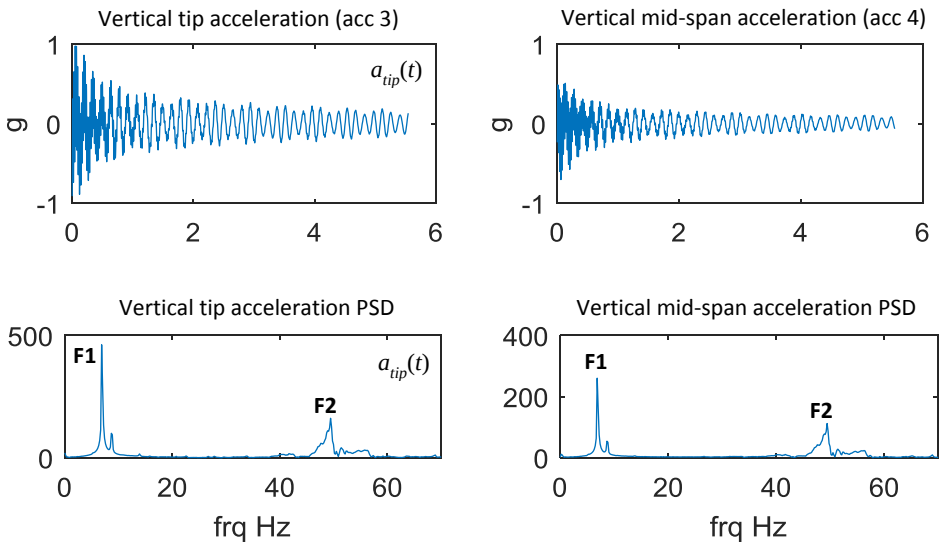

Figure 5: Typical tap-test accelerometer signals (time series subsets) and corresponding PSDs (time series in seconds, frequencies in Hz).

As well as the first two vertical bending modes, there is also another natural frequency just above **F1** which corresponds to the local and later unmodelled dynamics of the assembled beam-tank system.

The time series were then analysed using the ERA method described above. Figure 6 shows typical "stability plots" and damping vs frequency clusters for different sizes of the truncated analysis orders. System modes are defined in the stability plot as columns of red circles that indicate results that have stabilised in frequency and damping ratio and correspond with the power spectra and can be clearly seen in the cluster plot. The mean point in each cluster was taken as the estimated modal parameters for each mode.

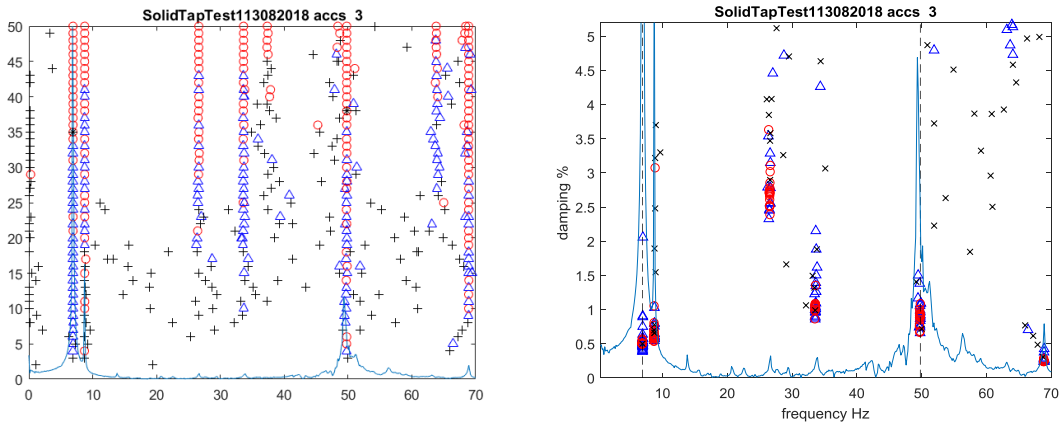

(a) (b)

Figure 6: Typical ERA identification: (a) Stability plot, (b) Damping vs. Frequency cluster plot.

Table 1 shows the results that were obtained from the analysis of each time series for the step release tests and tap tests, and also the overall averages and standard deviations for each set of tests. It can be seen that there is a good repeatability in the results from the analysis of the different time series and also between the two types of test. The scatter on the 2nd mode is greater than the 1st mode but this is due to the 2nd mode having a much smaller amplitude.

Table 1: Estimated frequencies and damping ratios of first two modes. Pull-release and tap tests.

13/08/2018	Mode 1 (**F1**)		Mode 2 (**F2**)	
	ω [Hz]	ζ [%]	ω [Hz]	ζ [%]
Test0 Solid *acc 3*	7.026	0.292	49.309	0.759
Test0 Solid *acc 4*	7.412	0.499	49.179	0.771
Test1 Solid *acc 3*	7.028	0.547	49.178	0.734
Test1 Solid *acc 4*	7.304	0.563	49.187	0.701
Test2 Solid *acc 3*	7.059	0.596	49.405	0.799
Test2 Solid *acc 4*	6.919	0.624	49.315	0.817
Average	*7.12*	*0.52*	*49.26*	*0.76*
Standard deviation	*0.19*	*0.12*	*0.09*	*0.04*
TapTest0 Solid *acc 1*	7.040	0.836	49.908	0.214
TapTest0 Solid *acc 2*	7.071	0.642	50.009	0.245
TapTest0 Solid *acc 3*	7.059	0.654	49.790	0.215
TapTest0 Solid *acc 4*	6.908	0.574	49.609	0.169
TapTest1 Solid *acc 1*	7.153	0.572	49.264	0.636
TapTest1 Solid *acc 2*	6.791	0.492	49.315	0.492
TapTest1 Solid *acc 3*	7.176	0.480	49.827	0.893
TapTest1 Solid *acc 4*	6.919	0.528	49.827	0.888
TapTest2 Solid *acc 1*	6.919	0.888	48.546	1.151
TapTest2 Solid *acc 2*	6.791	0.386	49.315	0.624
TapTest2 Solid *acc 3*	7.134	0.484	49.890	0.972
TapTest2 Solid *acc 4*	6.781	0.517	48.970	1.303
Average	*6.98*	*0.59*	*49.52*	*0.65*
Standard deviation	*0.15*	*0.15*	*0.45*	*0.39*

3.3 Nominal model with equivalent solid mass

A simplified finite element model has been employed to assess the modal properties for the structure and to provide a reliable quantification of the structural mass and stiffness distributions. This finite element model is also exploited to understand the local motion dynamics of the tank as given by the corresponding modal participation factors. The following results are provided for the case with the frozen liquid and full tanks. The first two mainly excited vibration mode shapes as given by a linear modal analysis are shown in Figure 7. Their nominal frequencies are 7.4 Hz and 52.81 Hz, respectively (*i.e.* the frequency ratio is about 7).

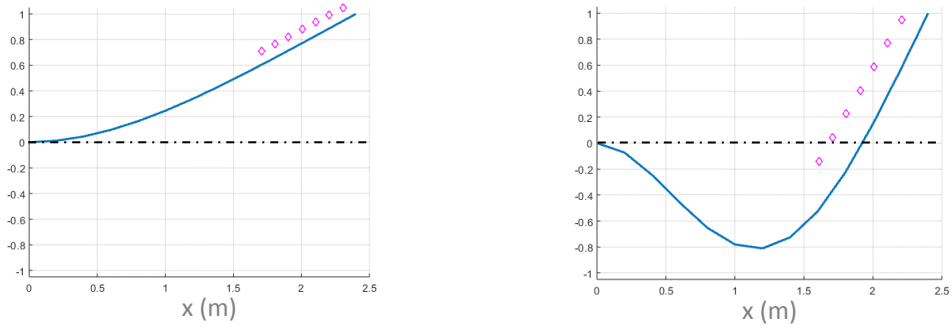

(a) (b)

Figure 7: Vibration mode shapes: (a) first mode **F1**, (b) second mode **F2**. Solid lines represent the beam centre lines, diamond markers indicate the full liquid container modelled as point mass elements.

The individual mode participation on the overall motion considered in the above experimental tests can provide useful hints to understand how the hydro-elastic coupling nonlinearly features in the structural behaviour. The motion of the tank due the first vibration mode **F1** consists of a marked vertical deflection able to trigger the Rayleigh-Taylor instabilities [12]. As far as the second mode **F2** is concerned, the tank centre position is close to the node of the second mode and, therefore, the consequent motion mainly consists of rotation and so the longitudinal deflection along the beam axis, thus providing the trigger for the lateral sloshing dynamics. Note that the interaction forces induced by these dynamics have a magnitude of second order as compared to those caused by the violent vertical sloshing.

By performing a linear static analysis to replicate the initial conditions set in the experiment (*i.e.* 7 cm vertical displacement at the tip), it has been found out that the modal participation factor (obtained by projecting the overall displacements on the actual mode shapes) of the tip vertical displacement is 6.83 cm and 0.32 cm for **F1** and **F2**, respectively. The total initial tip displacement is $d_0 = d_{0,1} + d_{0,2} + \cdots = 6.83\,cm + 0.32\,cm + \cdots \approx 7.0\,cm$. As expected, the imposed initial conditions excite mainly the first vibration mode (*i.e.* the initial condition ratio is about 21), and, in case of free harmonic oscillation, one has

$$d(t) = d_{0,1}\cos(\omega_1 t) + d_{0,2}\cos(\omega_2 t)\,. \tag{12}$$

However, considering the above decomposition for the tip point acceleration, one has

$$a(t) = -d_{0,1}\omega_1^2\cos(\omega_1 t) - d_{0,2}\omega_2^2\cos(\omega_2 t) = A_{0,1}\cos(\omega_1 t) + A_{0,2}\cos(\omega_2 t) \tag{13}$$

where $A_{0,1} = -147.65\ m/s^2$ and $A_{0,2} = -352.32\ m/s^2$. Therefore, these two acceleration modal participation factors are of the same order of magnitude.

4 DETAILED ANALYSIS

4.1 NLS analysis of F1 mode

Figure 4 provides preliminary indication of the non-stationary properties of the measured acceleration time series. To quantify these properties further, these data are subjected to the NLS analysis. Result of this analysis are the time-localized amplitude $A(t_i)$ and frequency $f(t_i)$ of the fitting function (7). The amplitudes $A(t_i)$ for the two selected data sets which correspond to the dry (0% filling) and wet (40% filling) conditions are presented in Figure 8.

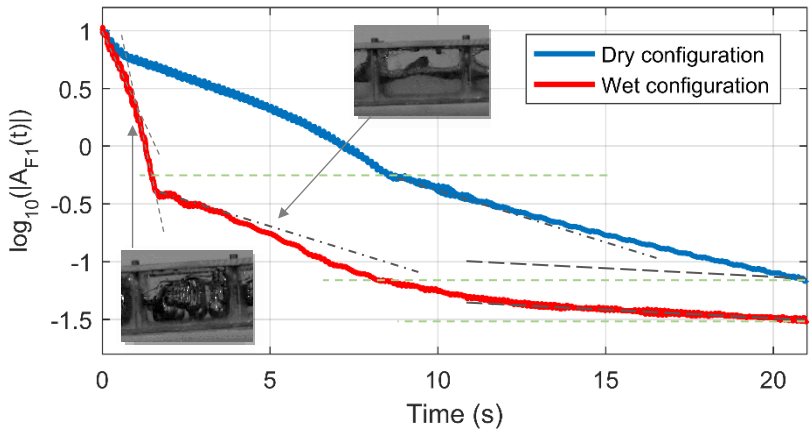

Figure 8: Comparison between the dry vs wet **F1** response envelopes.

The acceleration decay of the **F1** component in the wet configuration features significantly different trends when compared to the dry case. A set of superimposed lines is used to guide the eye, to highlight the trends and to facilitate the comparisons within and between the presented cases. The wet case is correlated with the recorded videos where the two distinct liquid sloshing modes are shown in two insets of this figure.

The initial violent sloshing leads to the liquid impacting against the top and bottom surfaces of the tank. Referring to Figure 7, this interaction pattern is mainly driven by the dominant vertical translational component embedded in **F1** mode. The vertical acceleration's decrease below a critical value triggers the end to this sloshing mode with the following liquid motion dominated by the longitudinal wave slamming and later moderate sloshing against the side walls of the tank. Referring to Figure 7, this interaction can be attributed to the tank's rotation about the nodal position of **F2** mode. Presence of the liquid in the system leads to a major difference between the vibration decay trends across these two cases. The slopes of the guiding lines indicate increased vibration decay occurring in multiple distinct stages before 10 s when the wet configuration starts an asymptotic approach to the lowest damping levels corresponding to the underlaying structural damping. This is not the case of the dry structure where all recoded stages appear to be dominated by the friction-driven energy dissipation of lower intensity.

Figure 9 aims to augment these insights with further quantitative analysis and correlation against the observed changes in $f(t_i)$. Considering the same wet configuration, Figure 9(a) shows the **F1** decay envelope in a natural logarithmic scale. Figure 9(b) shows the signal's time-frequency structure in the frequency region of interest. The black dashed lines in Figure 9(a), based on the local linear interpolation, facilitate precise damping ratio identification and guide further visual assessment. In particular, the intersection points between their consecutive instances broadly indicate an onset and transition between different fluid-structure interactional regimes. The resulting regions are identified as zones of interest ***A***, ***B***, ***C*** and ***D*** in Figure 9(b).

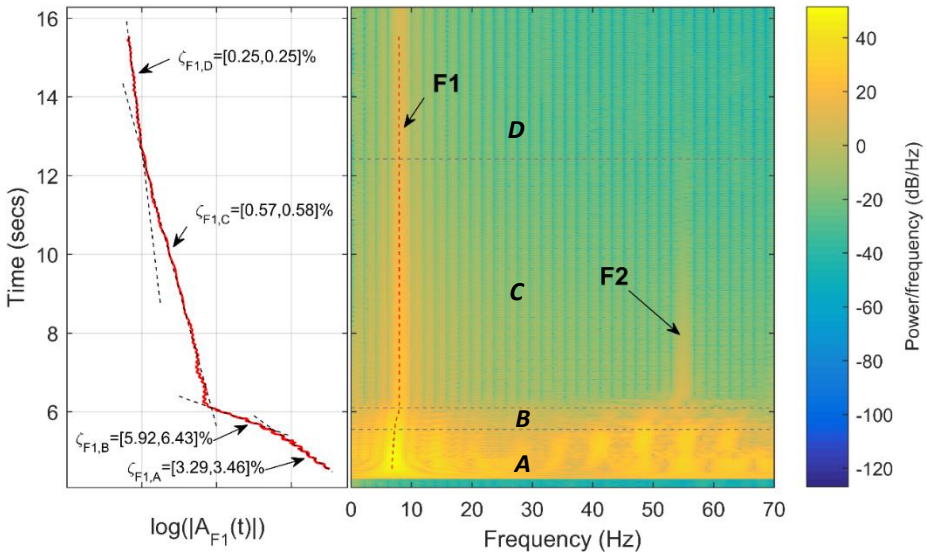

(a) (b)

Figure 9: Time-frequency analysis: a) decay envelope of mode **F1**, b) acceleration spectrogram.

While the presence of **F1** and **F2** is clearly observed in zones ***C*** and ***D***, the zones ***A*** and ***B*** also feature other nonlinear phenomena principally driven by mode **F1** and previously also observed in the dry test, see Figure 4. However, unlike the dry case, **F1** mode here undergoes additional time-localized frequency variation, as evidenced by the red dashed line, $f(t_i)$, in Figure 9(b), where the frequency drops significantly during the initial intense impacting sloshing. Figure 9(a) also reveals, through the nearly constant log-amplitude changes aligned with the black dashed lines, transitions between different energy-dissipation regimes.

Using approach explained in section 2.3, the equivalent "zonal" damping ratios reported in Figure 9(a) are identified while considering slow frequency **F1** variation within the regions. From comparison with Table 1, the local "zonal" damping ratio of 0.25 % corresponds to the underlaying structural damping at low vibration levels characteristic for zone ***D***, while the tap test results in Table 1 suggest higher more global damping ratio of 0.59 % identified at more widely varying levels of vibration with possible influences from friction and other effects.

As determined previously, due to the observed time-localized behaviour, a time domain system identification based on ERA and NLS is employed to determine the natural frequencies and damping ratios of each zone of interest. Based on Figure 9(a), it is assumed that frequency and damping remain constant in each response zone. The resulting frequency and damping values are given in Table 2.

Table 2: Estimated frequency and damping values for mode **F1**.

Zone	*ERA*		*NLS*[#]	
	ω (Hz)	ζ (%)	ω (Hz)	ζ (%)
A	6.93	4.50	6.97	3.38
B	7.32	5.55	7.60	6.18
C	8.00	0.62	7.96	0.58
D	7.97	0.71	7.95	0.25

[#] mean values used due to slow frequency variation within segments

The frequency changes between the different zones can be clearly seen, as indicated in the time-frequency plot in Figure 9(b). There is an order of magnitude damping difference between zones ***B*** and ***D***. There is also good agreement between the results obtained from the two methods.

The test cases for various filling ratios are systematically studied using the NLS approach. The corresponding **F1** zonal damping ratios for each test case are summarized in Figure 10. In addition, these quantities are compared in the same figure with the corresponding ERA-based **F1** damping ratio and its statistical spread. Owing to the shorter duration of these acceleration measurements, typically lasting 5 seconds, and with reference to Figure 8, this figure only reports on the damping values in zone ***A***, ***B*** and ***C***.

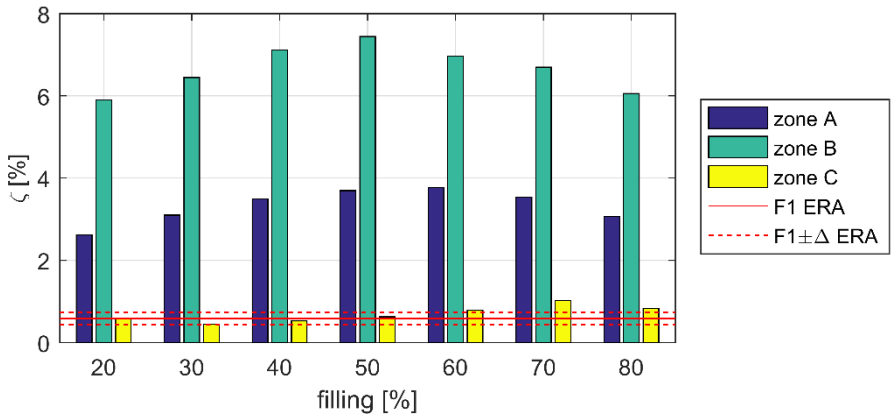

Figure 10: Identified damping zones with **F1** damping ratio obtained using NLS and ERA.

It is observed that the same zonal damping distribution pattern is maintained across different filling ratios. Further, the maximum damping ratios, both in zone ***A*** and ***B***, are reached for the filling ratio of 50 % which is in line with expected behaviour. The NLS damping ratios in zone ***C*** feature low damping values without characteristic filling-dependent trend while, at the same time, they match the ERA-based damping value and its spread obtained from Table 1. However, as discussed above, the NLS-based damping values are expected to decrease further in zone ***D***, due to the vanishing effect of liquid sloshing and friction, to the levels of the underlaying structural damping.

To motivate future research, the final study looks at the changing system behaviour under varying test configurations whilst keeping the same liquid filling ratio of 50%. For this study, summarized in Figure 11, three chosen cases are the nominal case with water, the case with kerosene instead of water, and the case with water and without internal walls.

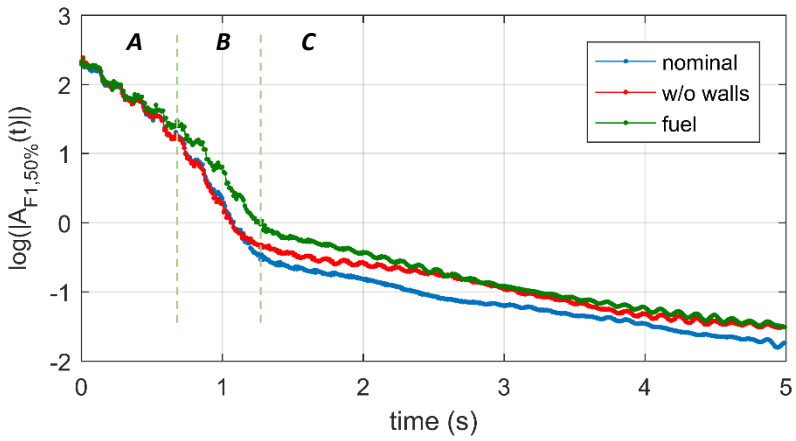

Figure 11: Energy dissipation according to **F1** response for 50% filling under varying test conditions.

Whilst not a statistically significant number of tests is demonstrated here, some key trends can be observed and used to motivate future design of experiments and model verification and validation studies. The initial stages of the measured response appear to be inertia-driven with similar energy dissipation intensity in zone ***A*** across all three configurations. This is followed by zone ***B*** where the vibration decay is maximized without significant differences between the compartmentalized (wall included) and open (no-walls) water-based configurations, suggesting thus dominant influence of the vertical wall-independent translational motion. This is contrasted by the response of the kerosene-filled configuration where the energy dissipation is slower (zone ***B***), characterized by the less steep slope of the acceleration response curve. This suggests the significance of the liquid properties in achieving particular levels of the maximized damping in zone ***B***. Following this, zone ***C*** highlights the significance of the separating walls in the liquid container. Here, initially intense vibration decay (zone ***B***) recorded for the case without the walls features the reduced slope in zone ***C*** while, at the same time, the water as well as kerosene-based cases with the walls demonstrate approximately parallel slopes of their respective acceleration responses in zone ***C***. This finding suggests that the increased number of interaction surfaces and shorter travel distances due to the separating walls during moderate longitudinal wave slamming, as influenced by the rocking motion originating from **F2** mode, increases the effective zonal damping.

This section presented insights based on the analysis associated with the vibration mode **F1**. To complete emerging picture, the next section focuses on the contribution and properties of the second mode **F2**.

4.2 WT analysis of F2 mode

In this section, WT analysis is employed to show **F2** response by improving the time-localization of its frequency content. WT is evaluated considering the first 4 seconds immediately after the initial release event. WT spectra are then obtained by means of Wavelet MATLAB toolbox [7]. In particular, the considered analyses involve: i) the comparison among the WT obtained from the experiments with frozen liquid case and the one with 30% filling level baffled tank; ii) the comparison among different filling level cases; iii) the extrapolation of the **F2** features by means of the interpolation process illustrated in section 2.3 and, finally, iv) the identification of specific sloshing signatures independent of different filling levels.

Concerning the first point above, Figure 12(a,b) shows the WT spectrum of the dry and wet (with 30% filling level) configurations, respectively. Note that in the following analyses the time and frequency axes order have been changed. It can be noticed that a raw time-frequency

trend of the **F1** response can be extrapolated from both figures as well. As with the previous NLS studies, WT analysis also indicates extreme increase in the damping levels due to liquid sloshing. On the other hand, as seen in Figure 4, **F2** response presents a behaviour extremely different from the one presented in section 3.1. The nonlinearities introduced to the system through the fluid-structure interactions, and other possible causes such as friction inside the system, are not presented by means of the super harmonic components. Instead, they are represented by the frequency and amplitude modulation represented in **F2** ridges (high frequency region).

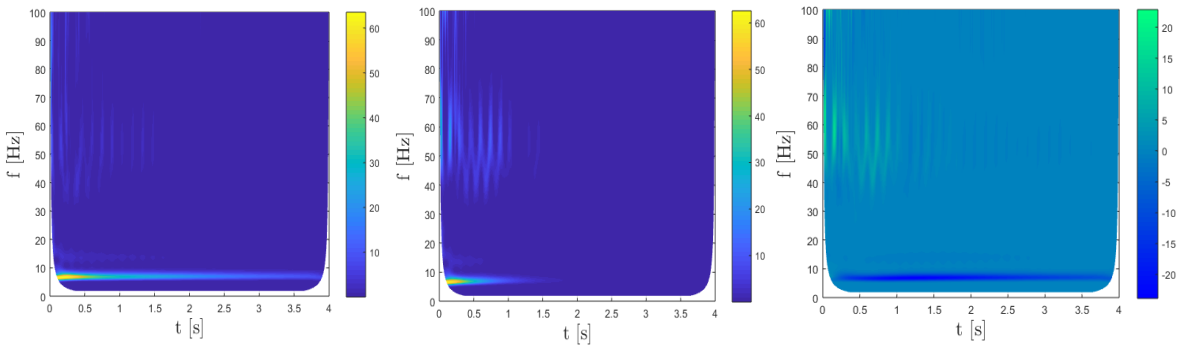

(a) (b) (c)

Figure 12: WT spectra of (a) dry, and (b) wet configurations with 30% filling level;
(c) dry-wet configuration difference.

The wet configuration shows a behaviour of **F2** that can be better interpreted by means of amplitude modulation rather than a frequency shift in time. Such impulsive excitation of **F2** is triggered by **F1** mode. This particular dry configuration behaviour could be explained by the presence of the friction-based interactions among the assembled components during the extremely violent response of the overall beam structure. On the other hand, for the case with sloshing, a true oscillation of the **F2** frequency occurs while the frequency **F1** is the modulating frequency of **F2** component. Figure 12(c) shows the difference between the two considered spectra. Though the fundamental vibration bending mode is more damped for the sloshing case (a negative ridge is present in the corresponding time-frequency slot), the difference between the spectra shows clearly that the excitation and the modulation of the **F2** component is mainly caused by the fluid-structure interaction.

The WT analysis is then applied to compare the responses with different filling levels in Figure 13. Generally, it can be noticed that as the filling level increases, the response of the **F2** component due to the fluid-structure interaction becomes weaker. In fact, the lower the filling level, the greater is the ability of the fluid to move and influence the instantaneous inertial characteristics of the structure. Furthermore, it can be noticed that the amplitude of this phenomenon does not have a purely decreasing trend, as it happens for the **F1** component. Instead, it can be seen that the response of **F2** is counter-intuitively triggered after 0.5 s.

The interpolation strategy illustrated in section 2.3 is applied then to track the variations in the **F2** component for each of the acceleration signals. Figure 14(a) shows the interpolated WT spectrum for the 30% filling level case as an example of the interpolation results. The identified frequencies ν_1 and ν_2 of the Gaussian functions, as well as their subtended areas A_1 and A_2 as obtained by the optimal problem in section 2.3, are shown in Figure 14(b,c).

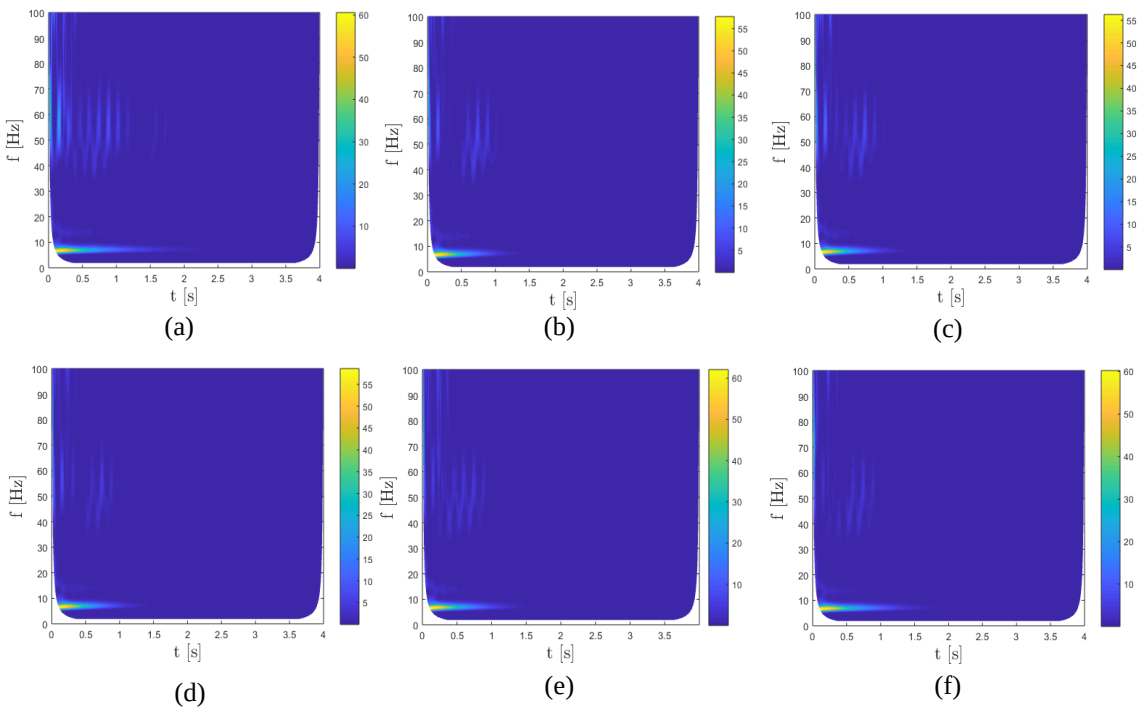

Figure 13: WT spectra with different filling levels: (a) 20%, (b) 40%, (c) 50%, (d) 60%, (e) 70%, (f) 80%.

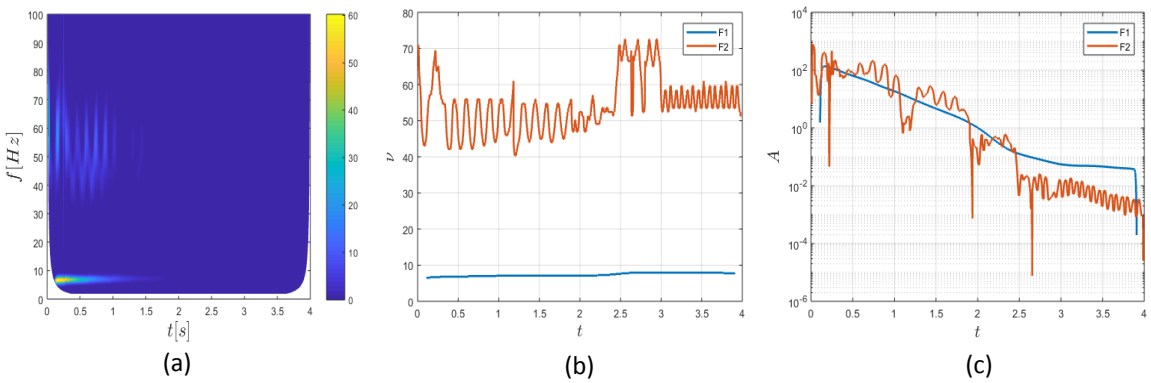

Figure 14: WT-based analysis: (a) spectrum interpolation, (b) identified frequency, and (c) amplitude.

Finally, it is worth pointing out that the behaviour of the identified frequency ν_2 is independent of the filling level in the time frame between 0 and 1.2 s, see Figure 15. Therefore, it can be considered as the sloshing signature. Further results of the cases already presented in section 4.1 do not show any qualitative difference when compared with the present WT-based analysis.

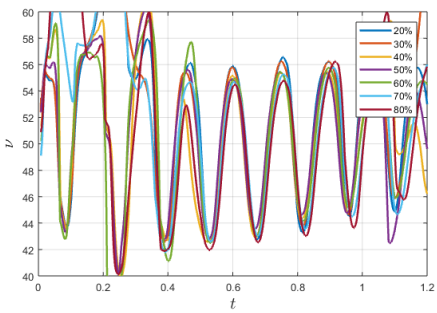

Figure 15: Frequency tracking for different filling levels between 0 and 1.2 s.

5 CONCLUSIONS

The liquid sloshing experiment on the scaled cantilever beam was developed to represent the sloshing fuel and elastic wing vibration interactions during transient events such as gusts. The research presented focused on systematic analysis of a selected subset of the measured acceleration responses obtained from the beam tip after its release from initially deformed position. This study focused mainly on the influence of the varying liquid filling ratio.

The preliminary study identified two bending modes of interest that were later closely studied with a combination of the three different time domain identification methods with the aim to understand their non-stationary dynamics. ERA was used to identify the underlaying nominal modal properties of the dry system and to provide an independent check for the NLS time-localized identification approach. NLS provided detailed information about the changes in the fundamental bending mode and WT was finally applied to develop a refined time and frequency-localized understanding of the second bending mode.

Both, dry and wet cases responded with complex behaviour characterized by a range of strong nonlinear phenomena. The dynamically tuned dry structure was mainly affected by friction and nonlinear stiffness originating from the liquid tank attachment to the beam. Additionally, the dynamically tuned wet structure was strongly affected by the liquid sloshing phenomena. In both configurations, the first two bending modes dominated the response and drove the nonlinear interactions. The presence of liquid was accompanied with the strong damping effects maximized at the 50% filling where the damping ratio rose from the underlaying approximate 0.3% structural damping to around 7.4% as a result of intense liquid-structure sloshing interactions. Furthermore, this interaction was the cause of the initial decrease in the fundamental vibration frequency from around 8 Hz to approximately 7 Hz.

This research delivered useful insights and practical experience when approaching and interpreting the relevant measured responses. The liquid-structure interaction in this setting introduced significant changes in the reference dry dynamic properties and it also introduced new interactional phenomena. The main notable finding is linked to the extent and mechanism associated with the maximum levels of the identified equivalent zonal damping ratios. Consequently, future effort will be aimed at completing further experimental, identification and simulation studies with the objective of identifying the key sensitive parameters and deeper understanding the limiting factors behind the achieved increased levels of damping.

6 REFERENCES

[1] Bouscasse, B., Colagrossi, A., Souto-Iglesias, A., and Cercos-Pita, J. L. (2014). Mechanical energy dissipation induced by sloshing and wave breaking in a fully coupled angular motion system. I. Theoretical formulation and numerical investigation. *Physics of Fluids*, 26(3), 033103-1 – 033103-21.

[2] Bouscasse, B., Colagrossi, A., Souto-Iglesias, A., and Cercos-Pita, J. L. (2014). Mechanical energy dissipation induced by sloshing and wave breaking in a fully coupled angular motion system. II. Experimental investigation. *Physics of Fluids*, 26(3), 033104-1 – 033104-22.

[3] Hall, J., Rendall, T. C. S., Allen, C. B., and Peel, H. (2015). A multi-physics computational model of fuel sloshing effects on aeroelastic behavior. *Journal of Fluids and Structures*, 56, 11 – 32.

[4] Konopka, M., De Rose, F., Strauch, H., Jetzschmann, C., Darkow, N., and Gerstmann, J. (2019). Active Slosh Control and Damping – Simulation and Experiment. *Acta Astronautica*, 158, 89 – 102.

[5] Fellowes, A., Wilson, T., Kemble, G., Havill, C., and Wright, J. (2011). Wing box non-linear structural damping. Proceedings of the *15th International Forum on Aeroelasticity and Structural Dynamics*, Paris, France, IFASD-2011-11, 1 – 20.

[6] Gambioli, F., Alegre Usach, R., Kirby, J., Wilson, T. and Behruzi, P. (2019). Experimental Evaluation of Fuel Sloshing Effects on Wing Dynamics, *Paper submitted to IFASD 2019*.

[7] Anonymous (2016). Matlab, Software Package, Version 9.0, MathWorks, Natick, MA.

[8] Juang, J. N. and Pappa, R. S. (1985). An eigensystem realization algorithm for modal parameter identification and model reduction. *Journal of Guidance, Control, and Dynamics*, 8(5), 620 – 627.

[9] Juang, J. N., Cooper, J. E., and Wright, J. R. (1988). An Eigensystem Realization Algorithm Using Data Correlations (ERA/DC) for Modal Parameter Identification. *Control – Theory and Advanced Technology*, 4(1), 5 – 14.

[10] Daubechies, I. (1990). The Wavelet Transform, Time-Frequency Localization and Signal Analysis. *IEEE Transactions on Information Theory*, 36(5), 961 – 1005.

[11] Rao, S. S. (2010). *Mechanical Vibrations*, 5th edition, Prentice Hall.

[12] Sharp, D. H. (1984). An overview of Rayleigh-Taylor instability. Physica D: Nonlinear Phenomena, 12(1–3), 3 – 10.

COPYRIGHT STATEMENT

The authors confirm that they, and/or their company or organization, hold copyright on all of the original material included in this paper. The authors also confirm that they have obtained permission, from the copyright holder of any third party material included in this paper, to publish it as part of their paper. The authors confirm that they give permission, or have obtained permission from the copyright holder of this paper, for the publication and distribution of this paper as part of the IFASD-2019 proceedings or as individual off-prints from the proceedings.